

ห้องสมุดงานวิจัย สำนักงานคณะกรรมการวิจัยแห่งชาติ



E47350



DIELECTRIC PROPERTIES OF NIO-BASED CERAMICS

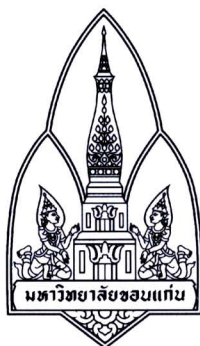
MR. PRASIT THONGBAI

A THESIS FOR THE DEGREE OF DOCTOR OF PHILOSOPHY
KHON KAEN UNIVERSITY

2010



E47350



DIELECTRIC PROPERTIES OF NiO-BASED CERAMICS



MR. PRASIT THONGBAI

**A THESIS FOR THE DEGREE OF DOCTOR OF PHILOSOPHY
KHON KAEN UNIVERSITY**

2010

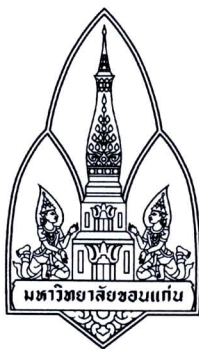
DIELECTRIC PROPERTIES OF NiO-BASED CERAMICS

MR. PRASIT THONGBAI

**A THESIS SUBMITTED IN PARTIAL FULFILLMENT OF THE
REQUIREMENTS FOR THE DEGREE OF DOCTOR OF PHILOSOPHY
IN PHYSICS**

GRADUATE SCHOOL KHON KAEN UNIVERSITY

2010



THESIS APPROVAL
KHON KAEN UNIVERSITY
FOR
DOCTOR OF PHILOSOPHY
IN PHYSICS

Thesis Title: Dielectric Properties of NiO-based Ceramics

Author: Mr. Prasit Thongbai

Thesis Examination Committee

Assoc. Prof. Dr. Vittaya Amornkitbamrung	Chairperson
Assoc. Prof. Dr. Santi Maensiri	Member
Assoc. Prof. Dr. Supon Ananta	Member
Dr. Teerapon Yamwong	Member
Dr. Samuk Pimanpang	Member

Thesis Advisors:

..... Advisor
(Assoc. Prof. Dr. Santi Maensiri)

..... Co-Advisor
(Dr. Teerapon Yamwong)

.....
(Assoc. Prof. Dr. Lampang Manmart)

Dean, Graduate School

.....
(Asst. Prof. Dr. Kiat Sangaroon)

Dean, Faculty of Science

ประสิทธิ์ ทองใบ. 2553. สมบัติทางไดอิเล็กตริกของวัสดุเซรามิกกลุ่ม NiO. วิทยานิพนธ์ปริญญา
ปรัชญาดุษฎีบัณฑิต สาขาวิชาฟิสิกส์ บัณฑิตวิทยาลัย มหาวิทยาลัยขอนแก่น.

อาจารย์ที่ปรึกษาวิทยานิพนธ์: รองศาสตราจารย์ ดร. สันติ แม้นศิริ,
ดร. ชีระพนธ์ เข้มวงษ์

บทคัดย่อ

E47350

ในงานวิจัยนี้ได้ศึกษาเพื่อหาจุดกำเนิดของการมีค่าคงที่ไดอิเล็กตริกที่สูงมากของ
วัสดุเซรามิก $\text{Li}_x\text{Ti}_y\text{Ni}_{1-x-y}\text{O}$ ($x = 0-0.10$ and $y = 0-0.15$) ที่เตรียมโดยวิธีพอร์ลิเมอร์ไลโรไลซิส
ได้ศึกษาลักษณะโครงสร้างผลึกโดยใช้เทคนิคการเลี้ยวเบนของรังสีเอกซ์ (XRD) ส่วนการศึกษา
โครงสร้างทางจุลภาคใช้กล้องจุลทรรศน์อิเล็กตรอนแบบส่องกราด (SEM) ร่วมกับเครื่องตรวจ
วิเคราะห์การกระจายพลังงาน (EDS) และได้ศึกษาสมบัติทางไดอิเล็กตริกและสมบัติทางไฟฟ้าของ
วัสดุเซรามิกในช่วงความถี่และอุณหภูมิต่างๆ

ผลการศึกษาโดยใช้เทคนิค XRD และ SEM-EDS ได้แสดงว่า ปริมาณการเจือของ Li และ
Ti มีผลกระทบอย่างมากต่อการเกิดเฟสและการเปลี่ยนแปลงของโครงสร้างทางจุลภาคของวัสดุ
เซรามิก $\text{Li}_x\text{Ti}_y\text{Ni}_{1-x-y}\text{O}$ ผลการทดลองพบว่า ไอออนของ Ti^{4+} ที่ใช้ในการเจือมีแนวโน้มที่จะรวมตัว
กับ NiO เกิดเป็นเฟสเจือปนของ NiTiO_3 ในขณะที่ไอออนของ Li^+ สามารถแทนที่ตำแหน่งไอออน
ของ Ni^{2+} ในโครงข่ายผลึกได้ และยังสามารถช่วยกระตุ้นให้ไอออนของ Ti^{4+} สามารถแทนที่
ตำแหน่งของ Ni^{2+} ได้เพิ่มมากขึ้น ผลการศึกษาโครงสร้างทางจุลภาคด้วยเทคนิค SEM-EDS ยืนยัน
ได้ว่าอนุภาคของ NiTiO_3 มีการสะสมอย่างมากที่ขอบเกรนและผิวหน้า อย่างไรก็ตาม เมื่อเพิ่ม
ปริมาณการเจือไอออนของ Li^+ อนุภาคของ NiTiO_3 จะไม่ปรากฏในโครงสร้างทางจุลภาค
การเปลี่ยนแปลงโครงสร้างทางจุลภาคดังกล่าวนี้สามารถอธิบายได้โดยใช้กลไกการเผาผนึกแบบ
เฟสของเหลว จากการศึกษาสมบัติทางไดอิเล็กตริกพบว่า วัสดุเซรามิก $\text{Li}_x\text{Ti}_y\text{Ni}_{1-x-y}\text{O}$ มีค่า
คงที่ไดอิเล็กตริกที่สูงมาก โดยมีค่าประมาณ 10^3-10^5 และพบว่าค่าคงที่ไดอิเล็กตริกมีค่าเพิ่มตาม
ขนาดของเกรนที่เพิ่มขึ้น กระบวนการผ่อนคลายทางไดอิเล็กตริกที่ความถี่ต่ำ (LFR) และที่ความถี่
สูง (HFR) สามารถเกิดขึ้นได้ในวัสดุเซรามิกที่มีปริมาณการเจือไอออนของ Ti^{4+} ที่สูง แต่ปริมาณ
ไอออนของ Li^+ ต่ำ ทั้งกระบวนการ LFR และ HFR สามารถอธิบายได้โดยการประยุกต์แบบจำลอง
การผ่อนคลายทางไดอิเล็กตริก Cole-Cole ร่วมกับพจน์ของการนำไฟฟ้ากระแสตรง ผลการศึกษา
อิทธิพลของชั้นผิวหน้าของวัสดุเซรามิก $\text{Li}_x\text{Ti}_y\text{Ni}_{1-x-y}\text{O}$ พบว่าการขัดผิวหน้าของวัสดุเซรามิก
ได้ส่งผลต่อกระบวนการ LFR แต่ไม่ส่งผลต่อ HFR จากผลการศึกษาด้วยเทคนิคอิมพีแดนซ์สามารถ
พิสูจน์ได้ว่า ชั้นผิวหน้าที่เกิดจากการสะสมของ NiTiO_3 มีสมบัติทางไฟฟ้าเป็นฉนวนและส่งผล
ต่อเนื่องถึงสมบัติทางไดอิเล็กตริกที่ความถี่ต่ำ เมื่อขัดชั้นฉนวนของผิวหน้าออก ค่าคงที่ไดอิเล็กตริก

E 47350

จะมีค่าลดลง แต่ค่าการสูญเสียทางไดอิเล็กตริกมีค่าเพิ่มขึ้น นอกจากนี้แล้วยังพบว่า ปริมาณของช่องว่างออกซิเจนในโครงสร้างมีผลอย่างมากต่อกระบวนการ LFR และ HFR หลังจากกระบวนการอบให้ความร้อนภายใต้บรรยากาศอาร์กอนเพื่อเพิ่มปริมาณช่องว่างของออกซิเจนพบว่า ความต้านทานรวมและความต้านทานของเกรนมีค่าเพิ่มมากขึ้น การเปลี่ยนแปลงค่าความต้านทานดังกล่าวนี้ได้ส่งผลกระทบต่อเนื่องถึงสมบัติทางไดอิเล็กตริกของวัสดุเซรามิกตัวอย่างเป็นอย่างมากทั้งในช่วงกระบวนการของ LFR และ HFR จากการศึกษาผลของชั้นฉนวนที่ผิวหน้าและการอบให้ความร้อนภายใต้บรรยากาศอาร์กอน แบบจำลองโครงสร้างทางจุลภาคได้ถูกสร้างขึ้นโดยอาศัยพื้นฐานของการโพลาไรเซชันที่ชั้นฉนวนภายในเพื่ออธิบายสมบัติทางไดอิเล็กตริกของวัสดุเซรามิก $\text{Li}_x\text{Ti}_y\text{Ni}_{1-x-y}\text{O}$

นอกเหนือจากการศึกษาเพื่อหาจุดเริ่มต้นของการมีค่าคงที่ไดอิเล็กตริกที่สูงมากของวัสดุเซรามิก $\text{Li}_x\text{Ti}_y\text{Ni}_{1-x-y}\text{O}$ แล้ว ในงานวิจัยนี้ยังได้ศึกษาสมบัติทางไดอิเล็กตริกของวัสดุเซรามิก $\text{Li}_x\text{Ti}_y\text{Ni}_{1-x-y}\text{O}$ ที่เตรียมโดยวิธีอื่นๆ และวัสดุเซรามิก NiO กลุ่มอื่นๆ คือ $\text{Li}_x\text{V}_y\text{Ni}_{1-x-y}\text{O}$ $\text{Li}_x\text{Fe}_y\text{Ni}_{1-x-y}\text{O}$ และ $\text{Li}_x\text{Al}_y\text{Ni}_{1-x-y}\text{O}$ ผลการทดลองพบว่า ค่าคงที่ไดอิเล็กตริกที่สูงมากของวัสดุเซรามิกกลุ่มดังกล่าวนี้สามารถอธิบายได้โดยใช้พื้นฐานของการโพลาไรเซชันที่ชั้นฉนวนภายในที่เกิดขึ้นในวัสดุเซรามิกที่มีโครงสร้างทางจุลภาคไม่สม่ำเสมอ ในงานวิจัยนี้ยังได้เปรียบเทียบสมบัติทางไดอิเล็กตริกของวัสดุเซรามิก $\text{Li}_{0.05}\text{Ti}_{0.02}\text{Ni}_{0.93}\text{O}$ กับวัสดุเซรามิก CuO บริสุทธิ์ ซึ่งเป็นวัสดุที่มีค่าคงที่ไดอิเล็กตริกที่สูงมากเหมือนกับวัสดุเซรามิกกลุ่ม NiO ต่างๆ โดยค่าคงที่ไดอิเล็กตริกที่สูงมากไม่เกี่ยวข้องกับสารเจือใดๆ พฤติกรรมทางไดอิเล็กตริกของวัสดุเซรามิก CuO สามารถอธิบายได้โดยใช้แบบจำลองการพ่นคลายทางไดอิเล็กตริกของ Cole-Cole นอกจากนี้ยังพบว่า ค่าคงที่ไดอิเล็กตริกมีค่าเพิ่มมากขึ้นตามขนาดของเกรนซึ่งเป็นลักษณะที่บ่งชี้ถึงการเกิดปรากฏการณ์ตัวเก็บประจุแบบชั้นขวางกันภายในในโครงสร้างทางจุลภาคของวัสดุเซรามิก CuO

Prasit Thongbai. 2010. **Dielectric Properties of NiO-based Ceramics**. Doctor of Philosophy Thesis in Physics, Graduate School, Khon Kaen University.

Thesis Advisors: Assoc. Prof. Dr. Santi Maensiri,
Dr. Teerapon Yamwong

ABSTRACT

E 47350

In this research, the origin of the giant dielectric response in $\text{Li}_x\text{Ti}_y\text{Ni}_{1-x-y}\text{O}$ ceramics ($x = 0-0.10$ and $y = 0-0.15$) prepared by a polymer pyrolysis method is investigated. X-ray diffraction (XRD) and scanning electron microscopy (SEM) with energy dispersive x-ray spectrometer (EDS) are used to characterize the phase composition and microstructure, respectively. The dielectric and electrical properties are investigated as functions of frequency and temperature.

The XRD and SEM-EDS results demonstrate that the Li and Ti doping concentrations have remarkable influences on both of the phase formation and microstructural evolution of the $\text{Li}_x\text{Ti}_y\text{Ni}_{1-x-y}\text{O}$ ceramics. It is found that the Ti^{4+} ions prefer to form the second phase of NiTiO_3 phase; in contrast, the Li^+ ions prefer to substitute the Ni^{2+} sites in the NiO crystal lattice. Interestingly, Li doping has a large contribution to the substitution of the Ti^{4+} ions on the Ni^{2+} sites. The surface morphologies and microstructure are found to be depended strongly on the Li and Ti doping concentrations. The SEM-EDS results show that the NiTiO_3 particles largely accumulate along the grain boundaries and surfaces. Surprisingly, such large accumulation can be erased by increasing the Li doping concentration. The microstructural evolution can suitably be ascribed based on the liquid-phase sintering mechanism. For the dielectric properties, it is revealed that all of the $\text{Li}_x\text{Ti}_y\text{Ni}_{1-x-y}\text{O}$ ceramics exhibit the giant dielectric constant, $\epsilon' \sim 10^3-10^5$. ϵ' of each ceramic composition increases with increasing the grain size. Two sets of relaxations are observed in the dielectric spectra of samples with high-Ti content and relative low-Li content. A low-frequency dielectric relaxation (LFR) is changed with the polishing surface; whereas, a high-frequency relaxation (HFR) remains constant. It can be proved that the NiTiO_3 surface layers behave as insulating layers, affecting to the LFR properties— ϵ' decreases with removing the insulating surfaces accompanied by the

E47350

increase in loss tangent. Both of the LFR and HFR can be well fitted by the Cole-Cole relaxation equation combined with the dc conduction term. It is found that the oxygen vacancies show a great influence on both of the LFR and HFR processes. The resistance of the grain of all samples increases with annealing of the samples in Ar. The total resistance of the group of samples that exhibit the LFR is found to be enhanced by the annealing. These changes in the resistances can cause a dramatic change in the dielectric properties in both the LFR and HFR processes. According to the investigation of the surface and annealing effects, two suitably models of the microstructure are proposed based on the interfacial polarization mechanism in order to describe the observed giant dielectric response in the $\text{Li}_x\text{Ti}_y\text{Ni}_{1-x-y}\text{O}$ ceramics.

Besides the investigation of the origin of the giant dielectric properties of the $\text{Li}_x\text{Ti}_y\text{Ni}_{1-x-y}\text{O}$ ceramics, the $\text{Li}_x\text{Ti}_y\text{Ni}_{1-x-y}\text{O}$ ceramics with different preparation methods and other NiO-based systems, i.e., (Li, Fe)-, (Li, V)-, and (Li, Al)-doped NiO systems, are also studied in this research. The giant dielectric properties of these ceramic systems can be ascribed based on the interfacial polarization mechanism, resulting from the inhomogeneous structure. Finally, the giant dielectric constant observed in the $\text{Li}_{0.05}\text{Ti}_{0.02}\text{Ni}_{0.93}\text{O}$ ceramic is compared to that observed in pure-CuO ceramic. Interestingly, the CuO ceramic can exhibit the giant dielectric properties without any dopants. Moreover, the dielectric relaxation behavior of the CuO ceramic can be ascribed by the Cole-Cole relaxation model just like the $\text{Li}_{0.05}\text{Ti}_{0.02}\text{Ni}_{0.93}\text{O}$ ceramic. Furthermore, it is found that the dielectric constant increases with increasing the grain size, suggesting to the internal barrier layer capacitor effect.

**Goodness portion of the present thesis is dedicated for
my family and all of my teachers**

ACKNOWLEDGEMENTS

I would like to express my deepest and sincere gratitude to my supervisor and co–advisor, Assoc. Prof. Dr. Santi Maensiri and Dr. Teerapon Yamwong for their relentless encouragement, constructive guidance and words of motivation throughout the duration of this research study and moreover for the inspiration they provided to ensure the completion of this work. Their expertise, availability to discuss ideas and willingness to give of their knowledge were instrumental. I am grateful to my PhD committee who took effort in reading and providing me with valuable comments: Assoc. Prof. Dr. Vittaya Amornkitbamrung, Assoc. Prof. Dr. Supon Ananta and Dr. Samuk Pimanpang.

I wish to thank the National Metal and Materials Technology Center (MTEC), Thailand for technical support in the dielectric constant and loss measurement. I have furthermore to thank the Department of Physics, Biology, and Chemistry, Faculty of Science at KKU, to use research facilities.

I would also like to express my thanks to my friends for their encouragement and thoughtful criticisms. I am also grateful for the help, assistance and friendship of the past and current students in the Small and Strong Materials Group (SSMG) members which will always be remembered with deep gratitude.

Finally, I would like to thank Ms. Nutthakritta Phromviyo for her great care, help, support and bringing me going through the good and bad times. My special thanks to my “Tongbai” family for the sacrifices they made, to bring me up and give the good life. Without their constant support and encouragement throughout my whole educational life, none of this would have been possible.

This research was supported by grant from The National Science and Technology Development Agency through the Thailand Graduate Institute of Science and Technology (TGIST) Programs and Graduate School, Khon Kaen University.

Prasit Thongbai

TABLE OF CONTENTS

	Page
ABSTRACT (IN THAI)	i
ABSTRACT (IN ENGLISH)	iii
DEDICATION	v
ACKNOWLEDGEMENTS	vi
TABLE OF CONTENTS	vii
LIST OF TABLES	xi
LIST OF FIGURES	xii
LIST OF SYMBOLS	xxviii
CHAPTER I INTRODUCTION	1
1.1 Principle and reason	1
1.2 Objectives of the research	3
1.3 Limitations of study	3
1.4 Location of the research	4
1.5 Anticipated outcomes	4
1.6 Structure of thesis	4
CHAPTER II THEORETICAL BACKGROUND	5
2.1 Basic dielectric theory	5
2.2 Polarizations in dielectrics	7
2.2.1 Electronic polarization	10
2.2.2 Atomic polarization	10
2.2.3 Orientational polarization	10
2.2.4 Space charge polarization	10
2.3 Dielectrics in alternating electric fields	11
2.4 Relationship between complex dielectric constant and polarization	14
2.5 Electric polarization and relaxation in time-varying electric field	17
2.6 Electric polarization and relaxation in alternating electric fields	24
2.7 Hopping polarization relaxation	29
2.8 Cole-Cole and other relaxation models	38

TABLE OF CONTENTS (Cont.)

	Page
2.9 The effect of dc conductivity on dielectric properties	40
2.10 Interfacial polarization	44
2.11 Temperature dependence of polarization	50
2.12 Impedance spectroscopy	52
2.13 Internal barrier layer capacitor model	56
CHAPTER III LITERATURE REVIEWS	59
3.1 Giant dielectric properties of Li and Ti co-doped NiO ceramics	59
3.2 Giant dielectric response in other NiO-based ceramic systems	68
3.3 Dielectric abnormalities in Zr-doped NiO ceramics	75
3.4 Effect of various valence states of the <i>A</i> -dopants on dielectric and electrical properties of the $A_{0.03}Ti_{0.10}Ni_{0.87}O$, where $A=K^+, Mg^{2+}, Y^{3+}$	77
3.5 Effect of various types of monovalent cations on the microstructure and dielectric properties of $A_{0.05}Ti_{0.02}Ni_{0.93}O$ ceramics, where $A=Li^+, Na^+, K^+$	79
3.6 High dielectric constant and low dielectric loss in (K, Ti)-doped NiO ceramics	81
3.7 Defects in (Li, Ti)-doped NiO ceramics system with giant dielectric constant	85
CHAPTER IV RESEARCH METHODOLOGY	87
4.1 Power and ceramic sample preparation	87
4.1.1 Synthesis of NiO-based powder and ceramic by polymer pyrolysis method	87
4.1.2 Synthesis of NiO-based powder and ceramic by direct thermal decomposition method	90
4.1.3 Synthesis of NiO-based powder and ceramic by PVA method	92
4.2 Powder and ceramic sample characterization	96

TABLE OF CONTENTS (Cont.)

	Page
4.2.1 X-ray diffraction (XRD)	96
4.2.2 Scanning electron microscopy (SEM)	97
4.2.3 Energy dispersive x-ray spectroscopy (EDS)	98
4.3 Dielectric and electrical properties measurement	99
CHAPTER V RESULTS AND DISCUSSION	101
5.1 Li and Ti co-doped NiO system	102
5.1.1 Powder characterization: morphologies and crystal structure	102
5.1.2 Ceramic characterization: crystal structure and morphologies	112
5.1.3 Temperature and frequency dependence of dielectric properties	158
5.1.4 Effect of sintering temperature on dielectric properties	172
5.1.5 Effect of dc conductivity on dielectric relaxation behavior	185
5.1.6 Electrical property: Impedance spectroscopy	189
5.1.7 Influence of interfaces on dielectric and electrical properties	196
5.1.8 Effect of annealing on dielectric and electrical properties	226
5.1.9 Possible origin(s) of the observed giant dielectric response in Li and Ti co-doped NiO ceramics	247
5.2 Li and Fe co-doped NiO system	282
5.3 Li and V co-doped NiO system	291
5.4 Effects of various valent states of doping ions on the microstructure and electrical properties of giant dielectric NiO-based ceramics	298
5.5 Dielectric and electrical properties of NiO-based ceramic systems prepared by a direct thermal decomposition method	305
5.5.1 Li and Ti co-doped NiO ceramics: Effect of sintering temperature on dielectric properties	305
5.5.2 Li and Al co-doped NiO ceramics	317
5.6 Dielectric and electrical properties of NiO-based ceramic systems prepared by a PVA method	326
5.6.1 Li and Fe co-doped NiO ceramics	326

TABLE OF CONTENTS (Cont.)

	Page
5.6.2 Li and Ti co-doped NiO ceramics	338
5.7 Comparison of giant dielectric properties of NiO-based and pure-CuO ceramics: Dielectric relaxation behavior	349
CHAPTER VI CONCLUSIONS AND SUGGESTIONS	357
6.1 Li and Ti co-doped NiO system	357
6.2 Li and Fe co-doped NiO system	359
6.3 Li and V co-doped NiO system	360
6.4 Effects of various valent states of doping ions on the microstructure and electrical properties giant dielectric NiO-based ceramics	360
6.5 Dielectric and electrical properties of NiO-based ceramic systems prepared by a direct thermal decomposition method	361
6.5.1 Li and Ti co-doped NiO ceramics: Effect of sintering temperature on dielectric properties	361
6.5.2 Li and Al co-doped NiO ceramics	361
6.6 Dielectric and electrical properties of NiO-based ceramic systems prepared by a PVA method	362
6.6.1 Li and Fe co-doped NiO ceramics	362
6.6.2 Li and Ti co-doped NiO ceramics	362
6.7 Comparison of giant dielectric properties of NiO-based and pure-CuO ceramics: Dielectric relaxation behavior	362
6.8 Suggestions	363
REFERENCES	365
APPENDICES	375
Appendix A Paper publications	377
Appendix B Presentations	379
VITAE	381

LIST OF TABLES

	Page
Table 3.1 The values of the dielectric constant (ϵ') at 1 kHz and room temperature and the activation energies of the $\text{Li}_x\text{Ti}_y\text{Ni}_{1-x-y}\text{O}$ ceramics.	67
Table 3.2 The values of the dielectric constant (ϵ') at 10 kHz and room temperature, the grain size, and the activation energies of the ZNO ceramics.	77
Table 3.3 The values of the dielectric constant (ϵ') at 1 kHz and room temperature and the activation energies of the $\text{A}_{0.03}\text{Ti}_{0.10}\text{Ni}_{0.87}\text{O}$ ceramics.	79
Table 3.4 The values of the dielectric constant (ϵ') and loss tangent $\tan\delta$ at 100 Hz and 300 K and the activation energies of the (K, Ti)-doped NiO ceramics.	83
Table 4.1 List of starting raw metallic materials, NiO-based ceramic samples, and sintering condition for three preparation methods.	94
Table 5.1 Lattice parameter of NiO, Li-doped NiO, Ti-doped NiO, and (Li, Ti)-doped NiO powders with different concentrations of Li and Ti doping ions.	108
Table 5.2 Lattice parameter of NiO, $\text{Ti}_y\text{Ni}_{1-y}\text{O}$, and $\text{Li}_x\text{Ti}_y\text{Ni}_{1-x-y}\text{O}$ ceramics sintered at 1200 and 1280 °C for 4 h.	114
Table 5.3 Average grain size of NiO, $\text{Ti}_y\text{Ni}_{1-y}\text{O}$, $\text{Li}_x\text{Ti}_{1-x}\text{O}$, and $\text{Li}_x\text{Ti}_y\text{Ni}_{1-x-y}\text{O}$ ceramics sintered at 1200 and 1280 °C for 4 h.	120
Table 5.4 Activation energy required for relaxation process (E_a) and the relaxation time at the upper limited temperature (τ_0) for the $\text{Li}_x\text{Ti}_y\text{Ni}_{1-x-y}\text{O}$ ceramics sintered at 1200 and 1280 °C for 4 h.	183
Table 5.5 Activation energy required for HFR process (E_a) of as-, polished-, air-, and Ar-samples of $\text{Li}_x\text{Ti}_y\text{Ni}_{1-x-y}\text{O}$ ceramics sintered at 1280 °C.	246
Table 5.6 Microstructure characteristics and phase compositions of $\text{Li}_x\text{Ti}_y\text{Ni}_{1-x-y}\text{O}$ ceramics sintered at 1280 °C.	248

LIST OF FIGURES

	Page
Figure 2.1 Charge on a parallel-plate capacitor with dielectric material between plates.	7
Figure 2.2 Frequency dependence of the polarization mechanisms in dielectrics.	9
Figure 2.3 Vector diagram of charging, loss, and total current in a dielectric.	12
Figure 2.4 The variation of different types of polarization with time under a step-function electric field.	18
Figure 2.5 The variation of different types of polarization with time under a step-function electric field.	21
Figure 2.6 The time response of $P(t)$ to a delta function electric field $E(u)$ of strength $E(u)$ within the time period of $u \leq t \leq u + du$.	23
Figure 2.7 Frequency dependence of dielectric properties of dielectric materials (plotted using equations (2.58)-(2.60)).	29
Figure 2.8 Potential well energy configuration in materials. The solid lines indicate energy without field; dot lines indicate energy with applied field.	30
Figure 2.9 Frequency dependence of dielectric properties of dielectric materials with different distributions of relaxation times obtained from Debye and Cole-Cole relaxation models (plotted using equation (2.104)).	40
Figure 2.10 Frequency dependence of dielectric loss ε'' represented by the Debye relaxation model, including the effect of dc conductivity. This figure shows the evolution of the relaxation process and dc conductivity contributing to the dielectric loss.	43

LIST OF FIGURES (Cont.)

	Page
Figure 2.11 Effect of dc conductivity σ_{dc} on dielectric relaxation behavior of dielectric materials. The dot lines represent only the loss component due to the effect of dc conductivity in order to compare with the total dielectric loss, which consists of the loss components due to the relaxation process and dc conductivity.	44
Figure 2.12 Schematic two-layer dielectric model comprising two materials, which have differences in electrical conductivity, thickness, and dielectric constant.	45
Figure 2.13 Frequency dependence of dielectric constant calculated from equation (2.127) for the system, as displayed in figure 2.12, with different values of σ_1 , σ_2 , ϵ'_1 , ϵ'_2 , d_1 , and d_2 .	49
Figure 2.14 Equivalent circuit used to represent the electrical properties of a polycrystalline ceramic material that exhibits grain (R_g, C_g) and grain-boundary (R_{gb}, C_{gb}) effects.	53
Figure 2.15 Construction of internal barrier layer capacitor model.	57
Figure 3.1 Temperature dependence of (a) dielectric constant (ϵ') and (b) loss tangent ($\tan\delta$) of the $\text{Li}_{0.05}\text{Ti}_{0.02}\text{Ni}_{0.93}\text{O}$ ceramic at various frequencies. The inset shows SEM image.	60
Figure 3.2 XRD pattern of the $\text{Li}_{0.10}\text{Ti}_{0.05}\text{Ni}_{0.85}\text{O}$ ceramic; inset (a) is Ti element profile obtained from the EDS spectra; inset (b) is the SEM image of the fractured surface of the $\text{Li}_{0.10}\text{Ti}_{0.02}\text{Ni}_{0.88}\text{O}$ ceramic.	61
Figure 3.3 Impedance spectra as a function of temperature for the $\text{Li}_{0.10}\text{Ti}_{0.05}\text{Ni}_{0.85}\text{O}$ ceramic; inset is the equivalent circuit. The small semicircle arc is displayed in the inset of the impedance spectrum at high frequency and 310 K.	63

LIST OF FIGURES (Cont.)

	Page
Figure 3.4	64
Figure 3.5	66
Figure 3.6	69
Figure 3.7	70
Figure 3.8	70
Figure 3.9	73
Figure 3.10	74
Figure 3.11	75

LIST OF FIGURES (Cont.)

	Page	
Figure 3.12	Frequency dependence of the dielectric constant (ϵ') at selected temperature for the $\text{Zr}_{0.1}\text{Ni}_{0.8}\text{O}$ ceramic; inset shows the frequency dependence of dielectric constant of the $\text{Zr}_{0.2}\text{Ni}_{0.6}\text{O}$ ceramic.	76
Figure 3.13	Temperature dependence of the dielectric constant (ϵ') of the $\text{Y}_{0.03}\text{Ti}_{0.10}\text{Ni}_{0.87}\text{O}$ ceramic at selected frequencies.	78
Figure 3.14	(a)-(c) SEM images of the surface morphologies of the NaTNO, KTNO, and LTNO ceramics, respectively. (d) Frequency dependence of the dielectric constant (ϵ') at room temperature for the NiO-based ceramics doping with various monovalents.	81
Figure 3.15	Temperature dependence of (a) the dielectric constant (ϵ') and (b) the loss tangent ($\tan\delta$) of the $\text{K}_{0.05}\text{Ti}_{0.02}\text{Ni}_{0.93}\text{O}$ ceramic at different frequencies.	82
Figure 3.16	Frequency dependence of the dielectric properties of the $\text{K}_{0.05}\text{Ti}_{0.02}\text{Ni}_{0.93}\text{O}$ ceramic at various temperatures: the real (ϵ') and imaginary (ϵ'') parts of the complex permittivity ($\epsilon^*=\epsilon'-j\epsilon''$) and the loss tangent ($\tan\delta=\epsilon''/\epsilon'$). The inset shows the Arrhenius plot of the relaxation process.	84
Figure 4.1	Diagram showing preparation and characterization of NiO-based powder and ceramic synthesized by the polymer pyrolysis method.	89
Figure 4.2	Diagram showing preparation and characterization of NiO-based powder and ceramic synthesized by the direct thermal decomposition method.	91
Figure 4.3	Diagram showing preparation and characterization of NiO-based powder and ceramic synthesized by the PVA method.	93

LIST OF FIGURES (Cont.)

	Page
Figure 4.4	Diagram showing measuring dielectric parameters of the NiO-based ceramic samples using a Hewlett Packard 4194A impedance gain phase analyzer.
	100
Figure 5.1	SEM images of NiO and $\text{Li}_x\text{Ti}_y\text{Ni}_{1-x-y}\text{O}$ powders with different concentrations of Li (x) and Ti (y) doping ions.
	103
Figure 5.2	XRD patterns of the powders for NiO and Li-doped NiO with different concentrations of Li doping ions, Li = 2, 5, and 10 mol %.
	106
Figure 5.3	XRD patterns of NiO and Ti-doped NiO powders with different concentrations of Ti doping ions, Ti = 2, 5, 10, and 15 mol %.
	109
Figure 5.4	XRD patterns of $\text{Li}_x\text{Ti}_y\text{Ni}_{1-x-y}\text{O}$ powders with different concentrations of Li and Ti doping ions; (a) group 3 and (b) group 4.
	110
Figure 5.5	XRD patterns of NiO and $\text{Ti}_y\text{Ni}_{1-y}\text{O}$ ceramics sintered at (a) 1200 °C and (b) 1280 °C.
	113
Figure 5.6	XRD patterns of $\text{Li}_x\text{Ti}_y\text{Ni}_{1-x-y}\text{O}$ ceramics sintered at 1200 °C [(a) and (b)] and 1280 °C [(c) and (d)].
	115
Figure 5.7	SEM images of $\text{Ti}_y\text{Ni}_{1-y}\text{O}$ ceramics sintered at 1200 °C revealing the surface morphologies; inset is its higher magnification image.
	121
Figure 5.8	SEM images of $\text{Ti}_y\text{Ni}_{1-y}\text{O}$ ceramics sintered at 1280 °C revealing the surface morphologies; inset is its higher magnification image.
	124
Figure 5.9	(a) SEM image and (b)-(e) EDS spectra of the testing points 1-4 for the $\text{Ti}_{0.02}\text{Ni}_{0.98}\text{O}$ ceramic sintered at 1280 °C.
	127
Figure 5.10	SEM images of $\text{Li}_x\text{Ni}_{1-x}\text{O}$ ceramics sintered at 1280 °C revealing the surface morphologies; inset is its higher magnification image.
	130

LIST OF FIGURES (Cont.)

	Page
Figure 5.11 SEM images of $\text{Li}_{0.05}\text{Ti}_y\text{Ni}_{0.95-y}\text{O}$ ceramics ($y = 0.02, 0.05, 0.10$, and 0.15) sintered at $1200\text{ }^\circ\text{C}$; inset shows its higher magnification image.	134
Figure 5.12 SEM images of $\text{Li}_{0.05}\text{Ti}_y\text{Ni}_{0.95-y}\text{O}$ ceramics ($y = 0.02, 0.05, 0.10$, and 0.15) sintered at $1280\text{ }^\circ\text{C}$; inset shows its higher magnification image.	136
Figure 5.13 (a) SEM image and (b)-(c) EDS spectra of the testing points 1 and 2 for the $\text{Li}_{0.05}\text{Ti}_{0.02}\text{Ni}_{0.93}\text{O}$ ceramic sintered at $1280\text{ }^\circ\text{C}$.	141
Figure 5.14 (a) SEM image and (b)-(c) EDS spectra of the testing points 1 and 2 for the $\text{Li}_{0.05}\text{Ti}_{0.05}\text{Ni}_{0.90}\text{O}$ ceramic sintered at $1280\text{ }^\circ\text{C}$.	142
Figure 5.15 (a) SEM image and (b)-(c) EDS spectra of the testing points 1 and 2 for the $\text{Li}_{0.05}\text{Ti}_{0.10}\text{Ni}_{0.85}\text{O}$ ceramic sintered at $1280\text{ }^\circ\text{C}$.	143
Figure 5.16 (a) SEM image and (b)-(c) EDS spectra of the testing points 1 and 2 for the $\text{Li}_{0.05}\text{Ti}_{0.15}\text{Ni}_{0.80}\text{O}$ ceramic sintered at $1280\text{ }^\circ\text{C}$.	144
Figure 5.17 SEM images of $\text{Li}_x\text{Ti}_{0.05}\text{Ni}_{0.95-x}\text{O}$ ($x = 0.02, 0.05$, and 0.10) and $\text{Li}_{0.10}\text{Ti}_{0.02}\text{Ni}_{0.88}\text{O}$ ceramics sintered at $1200\text{ }^\circ\text{C}$; inset shows its higher magnification image.	146
Figure 5.18 SEM images of $\text{Li}_x\text{Ti}_{0.05}\text{Ni}_{0.95-x}\text{O}$ ($x = 0.02, 0.05$, and 0.10) and $\text{Li}_{0.10}\text{Ti}_{0.02}\text{Ni}_{0.88}\text{O}$ ceramics sintered at $1280\text{ }^\circ\text{C}$; inset shows its higher magnification image.	148
Figure 5.19 (a) SEM image and (b)-(c) EDS spectra of the testing points 1 and 2 for the $\text{Li}_{0.02}\text{Ti}_{0.05}\text{Ni}_{0.93}\text{O}$ ceramic sintered at $1280\text{ }^\circ\text{C}$; inset is in (b) shows the EDS spectrum of the testing point 3.	151

LIST OF FIGURES (Cont.)

	Page
Figure 5.20 SEM-EDS results of the testing points at a grain and grain boundary for (a), (b) $\text{Li}_{0.10}\text{Ti}_{0.05}\text{Ni}_{0.85}\text{O}$ and (c), (d) $\text{Li}_{0.10}\text{Ti}_{0.02}\text{Ni}_{0.98}\text{O}$ ceramics sintered at 1280 °C.	152
Figure 5.21 Temperature dependence of dielectric constant (ϵ') and loss tangent ($\tan\delta$) at the frequency range of 10^2 - 10^6 Hz for $\text{Li}_x\text{Ti}_y\text{Ni}_{1-x-y}\text{O}$ ceramics sintered at 1200 °C.	160
Figure 5.22 Frequency dependence of dielectric properties (dielectric constant (ϵ'), loss tangent ($\tan\delta$), and dielectric loss (ϵ'')) at the temperature range of -60 to 60 °C for $\text{Li}_x\text{Ti}_y\text{Ni}_{1-x-y}\text{O}$ ceramics sintered at 1200 °C.	165
Figure 5.23 (a)-(d) Dielectric constant (ϵ') and (e)-(h) dielectric loss (ϵ'') of the $\text{Li}_{0.05}\text{Ti}_y\text{Ni}_{0.95-y}\text{O}$ ceramics sintered at 1200 and 1280 °C.	174
Figure 5.24 Frequency dependence of dielectric properties (dielectric constant (ϵ'), loss tangent ($\tan\delta$), and dielectric loss (ϵ'')) at the temperature range of -60 to 60 °C for $\text{Li}_x\text{Ti}_y\text{Ni}_{1-x-y}\text{O}$ ceramics sintered at 1280 °C.	175
Figure 5.25 Temperature dependence of relaxation time of $\text{Li}_x\text{Ti}_y\text{Ni}_{1-x-y}\text{O}$ ceramics sintered at (a) 1200 and (b) 1280 °C; the solid lines are the data fitted by an Arrhenius law.	184
Figure 5.26 Dielectric spectra of $\text{Li}_x\text{Ti}_y\text{Ni}_{1-x-y}\text{O}$ ceramics sintered at 1280 °C fitting to equation (5.10); inset shows dielectric loss and fitted results.	187
Figure 5.27 Impedance spectra of $\text{Ti}_y\text{Ni}_{1-y}\text{O}$ and $\text{Li}_x\text{Ti}_y\text{Ni}_{1-x-y}\text{O}$ ceramics sintered at 1200 °C at various temperatures; inset shows its impedance spectrum at -60 °C.	192
Figure 5.28 Impedance spectra of $\text{Li}_{0.05}\text{Ti}_{0.02}\text{Ni}_{0.93}\text{O}$ ceramic sintered at 1200 °C at temperatures of (a) 60 °C and (b) -60 °C fitted by equations (5.12) and (5.15).	195

LIST OF FIGURES (Cont.)

	Page
Figure 5.29 Dielectric constant (ϵ') and loss tangent ($\tan\delta$) at 30 °C of $\text{Li}_x\text{Ti}_y\text{Ni}_{1-x-y}\text{O}$ ceramics sintered at 1280 °C for non- (as-) and polished-samples; inset is the dielectric properties at -40 °C.	201
Figure 5.30 SEM images of surface morphologies of $\text{Li}_x\text{Ti}_y\text{Ni}_{1-x-y}\text{O}$ as- and polished-samples sintered at 1280 °C for group-I.	208
Figure 5.31 SEM images of surface morphologies of $\text{Li}_x\text{Ti}_y\text{Ni}_{1-x-y}\text{O}$ as- and polished-samples sintered at 1280 °C for group-II.	209
Figure 5.32 SEM images of surface morphologies of $\text{Li}_x\text{Ti}_y\text{Ni}_{1-x-y}\text{O}$ as- and polished-samples sintered at 1280 °C for group-III.	210
Figure 5.33 Complex impedance plane plot at 30 °C of $\text{Li}_x\text{Ti}_y\text{Ni}_{1-x-y}\text{O}$ ceramics sintered at 1280 °C for non- (as-) and polished-samples; inset is an expanded view of high frequency data close to the origin.	217
Figure 5.34 Low-frequency relaxation (LFR) and high-frequency relaxation (HFR) of (a) $\text{Li}_{0.05}\text{Ti}_{0.05}\text{Ni}_{0.90}\text{O}$ and (b) $\text{Li}_{0.05}\text{Ti}_{0.15}\text{Ni}_{0.80}\text{O}$ ceramics sintered at 1280 °C at various temperatures; the solid and dot curves are the best fit to Cole-Cole relaxation model for the LFR and HFR, respectively.	224
Figure 5.35 The evolution of the relaxation and dc conductivity contributed to the total loss tangent at -40 °C for the as-sample for $\text{Li}_{0.05}\text{Ti}_{0.15}\text{Ni}_{0.80}\text{O}$ ceramic sintered at 1280 °C; the red solid curve and the blue dot curve are respectively the best fit to Eq. (5.10) for HFR and the expected LFR estimated by the Cole-Cole relaxation model (Eq. (5.18)).	225
Figure 5.36 Arrhenius plot of the LFR of the as-samples for the $\text{Li}_{0.05}\text{Ti}_{0.05}\text{Ni}_{0.90}\text{O}$ $\text{Li}_{0.05}\text{Ti}_{0.15}\text{Ni}_{0.80}\text{O}$ ceramics sintered at 1280 °C.	225

LIST OF FIGURES (Cont.)

	Page
Figure 5.37 Frequency dependence of dielectric properties at 30 °C for as-sample, polished-sample, and Ar-sample of $\text{Li}_x\text{Ti}_y\text{Ni}_{1-x-y}\text{O}$ ceramics sintered at 1280 °C for 4 h; inset shows the frequency dependence of the dielectric constant of these four samples at -40 °C.	230
Figure 5.38 Complex impedance plane plot at 30 °C of $\text{Li}_x\text{Ti}_y\text{Ni}_{1-x-y}\text{O}$ ceramics sintered at 1280 °C for as-sample, polished-sample, and Ar-sample; inset is an expanded view of high frequency data close to the origin.	238
Figure 5.39 Frequency dependence of dielectric properties at various temperatures for Ar-samples of $\text{Li}_x\text{Ti}_y\text{Ni}_{1-x-y}\text{O}$ ceramics sintered at 1280 °C for 4 h.	244
Figure 5.40 Frequency dependence of dielectric properties at -60 °C for Ar-samples of $\text{Li}_x\text{Ti}_y\text{Ni}_{1-x-y}\text{O}$ ceramics sintered at 1280 °C for 4 h.	246
Figure 5.41 Schematics of (a) NiO, (b) Li-doped NiO, and (c) Ti-doped NiO, showing the formation of defect.	250
Figure 5.42 (a) Idealized ceramic microstructure of the brick-well model or IBLC structure model, and (b) Equivalent circuit corresponding to the microstructure model.	253
Figure 5.43 Impedance spectrum at 120 °C for the $\text{Li}_{0.10}\text{Ti}_{0.05}\text{Ni}_{0.85}\text{O}$ ceramic (polished-sample) sintered at 1280 °C fitted by equation (5.15); inset shows the fitted result at -60 °C.	254
Figure 5.44 (a) Idealized ceramic microstructure of the IBLC/SBLC structure model, and (b) Equivalent circuit corresponding to the microstructure model.	257
Figure 5.45 Impedance spectra at 30 °C of (a) $\text{Li}_{0.05}\text{Ti}_{0.05}\text{Ni}_{0.90}\text{O}$ and (b) $\text{Li}_{0.05}\text{Ti}_{0.15}\text{Ni}_{0.80}\text{O}$ ceramics (as-samples) sintered at 1280 °C fitted by equation (5.24); inset shows an expanded view of high frequency data close to the origin.	258

LIST OF FIGURES (Cont.)

	Page
Figure 5.46 Impedance spectra of (a) $\text{Li}_{0.05}\text{Ti}_{0.05}\text{Ni}_{0.90}\text{O}$ and (b) $\text{Li}_{0.05}\text{Ti}_{0.15}\text{Ni}_{0.80}\text{O}$ ceramics (as- and polished-samples) fitted by equation (5.24) using the same parameters as revealed in Table 5.7, but given $R_s=0$.	259
Figure 5.47 Frequency dependence of dielectric constant (ϵ') of $\text{Li}_x\text{Ti}_y\text{Ni}_{1-x-y}\text{O}$ ceramics sintered at 1280 °C for as- and polished-samples; inset shows surface morphology.	262
Figure 5.48 Schematics of (a) NiO and Li-doped NiO structure with different types of charge compensation: (b) oxygen vacancy and (c) Ni^{3+} , respectively.	266
Figure 5.49 (a) Schematics of Li-doped NiO structure with oxygen compensation and (b) the related band structure.	269
Figure 5.50 Schematics of Li-doped NiO structure with Ni^{3+} compensation: (a) before annealing and (b) after annealing.	270
Figure 5.51 Schematics of the changes in (a) electrostatic potential and (b) defect concentrations as a function of distance from grain boundary for the segregation of the Ti doping ions in $\text{Li}_x\text{Ti}_y\text{Ni}_{1-x-y}\text{O}$ ceramics.	272
Figure 5.52 Microstructural models proposed for $\text{Li}_x\text{Ti}_y\text{Ni}_{1-x-y}\text{O}$ ceramics; (a) double-IBLC/SBLC model and (b) IBLC model.	274
Figure 5.53 Effect of annealing on the microstructure the double-IBLC/SBLC model for the polished-samples.	278
Figure 5.54 Dielectric constant and loss tangent of the $\text{Li}_{0.05}\text{Ti}_{0.15}\text{Ni}_{0.80}\text{O}$ ceramic fitted by equation (5.27); (a) polished-sample and (b) Ar-sample.	279
Figure 5.55 The dependence of the dielectric constant at 30 °C and 10^5 Hz on the concentration of Li and Ti doped in $\text{Li}_x\text{Ti}_y\text{Ni}_{1-x-y}\text{O}$ ceramics (polished-samples).	281

LIST OF FIGURES (Cont.)

		Page
Figure 5.56	(a) Fractured surface of the $\text{Li}_{0.05}\text{Fe}_{0.10}\text{Ni}_{0.85}\text{O}$ sample and (b) shows Ni and Fe element profiles obtained from the EDS spectra at different points; inset shows SEM image of surface morphology.	284
Figure 5.57	Frequency dependence of (a) dielectric constant and loss tangent for LFNO-1Be (symbols) and LFNO-1Af (solid lines) samples at various temperatures from -40 to 200 °C with the step increase in temperature is 30 °C.	285
Figure 5.58	(a) Impedance spectra of LFNO samples before and after surface polishing at 20 °C. (b) Impedance spectra as a function of dc bias of LFNO-1Be; inset shows impedance spectra of LFNO-1Af.	287
Figure 5.59	Frequency dependence of dielectric constant at various applied voltages at room temperature for LFNO-1Af sample; inset shows its frequency dependence of loss tangent at different applied voltages.	288
Figure 5.60	Frequency dependence of Z'' at various temperatures for LFNO-1Af sample. Inset shows the frequency dependence of Z'' at different applied voltages for LFNO-1Af sample.	290
Figure 5.61	XRD patterns of the LVNO powders and sintered ceramics; (a) $\text{Li}_{0.05}\text{V}_{0.02}\text{Ni}_{0.93}\text{O}$ (b), $\text{Li}_{0.05}\text{V}_{0.05}\text{Ni}_{0.90}\text{O}$, and (c) $\text{Li}_{0.05}\text{V}_{0.10}\text{Ni}_{0.85}\text{O}$; (d) is XRD pattern of $\text{Li}_{0.05}\text{V}_{0.10}\text{Ni}_{0.85}\text{O}$ with polished surface.	291
Figure 5.62	The element profile obtained from EDS spectra.	292
Figure 5.63	Frequency dependence of (a) the dielectric constant (ϵ') and (b) dielectric loss (ϵ'') at different temperatures. Inset is the temperature dependence of the relaxation time for the different LVNO samples.	293

LIST OF FIGURES (Cont.)

	Page
Figure 5.64 Temperature dependence of relaxation times of LVNO ceramics.	294
Figure 5.65 Impedance spectra as a function of temperature for the $\text{Li}_{0.05}\text{V}_{0.10}\text{Ni}_{0.85}\text{O}$ ceramic; inset shows impedance spectra at a low-temperature range.	294
Figure 5.66 Temperature dependence of grain (a) and (b) grain boundary conductivity.	296
Figure 5.67 SEM images of the surfaces for the (a) $\text{Li}_{0.05}\text{Ti}_{0.02}\text{Ni}_{0.93}\text{O}$, (b) $\text{Li}_{0.05}\text{Fe}_{0.02}\text{Ni}_{0.93}\text{O}$, and (c) $\text{Li}_{0.05}\text{V}_{0.02}\text{Ni}_{0.93}\text{O}$ ceramics; inset of Fig. 5.67(c) shows the fractured surface of the LVNO sample. (d) EDS spectra of the grains and grain boundary for $\text{Li}_{0.05}\text{V}_{0.02}\text{Ni}_{0.93}\text{O}$ ceramic.	299
Figure 5.68 Frequency dependence of dielectric constant and loss tangent at 30°C for the $\text{Li}_{0.05}\text{Ti}_{0.02}\text{Ni}_{0.93}\text{O}$, $\text{Li}_{0.05}\text{Fe}_{0.02}\text{Ni}_{0.93}\text{O}$, and $\text{Li}_{0.05}\text{V}_{0.02}\text{Ni}_{0.93}\text{O}$ ceramics. (b) The temperature dependence of dielectric constant at selected frequencies for the $\text{Li}_{0.05}\text{V}_{0.02}\text{Ni}_{0.93}\text{O}$ ceramic.	301
Figure 5.69 The complex impedance plane plots for the (a) $\text{Li}_{0.05}\text{V}_{0.02}\text{Ni}_{0.93}\text{O}$ and (b) $\text{Li}_{0.05}\text{Ti}_{0.02}\text{Ni}_{0.93}\text{O}$ ceramics at various temperatures; insets show the corresponding impedance spectra at low temperatures. (c) and (d) are the Arrhenius plots of the conductivities of the grains and grain boundaries, respectively.	302
Figure 5.70 XRD patterns of $\text{Li}_{0.05}\text{Ti}_{0.02}\text{Ni}_{0.93}\text{O}$ powder and ceramics sintered at 1200 and 1280 °C.	307
Figure 5.71 SEM images of surface morphologies of $\text{Li}_{0.05}\text{Ti}_{0.02}\text{Ni}_{0.93}\text{O}$ ceramics sintered at (a) 1200 and (b) 1280 °C.	308
Figure 5.72 SEM images of surface morphologies of $\text{Li}_{0.05}\text{Ti}_{0.02}\text{Ni}_{0.93}\text{O}$ ceramics sintered at (a) 1200 and (b) 1280 °C.	309

LIST OF FIGURES (Cont.)

		Page
Figure 5.73	(a) and (c) Temperature dependence of ε' for the LTNO-1 and LTNO-2, respectively. (b) and (d) Temperature dependence of $\tan\delta$ for the LTNO-1 and LTNO-2, respectively.	310
Figure 5.74	(a), (c) Frequency dependence of dielectric constant for the ceramics sintered at 1200 and 1280 °C, respectively. (b), (d) Frequency dependence of dielectric loss (ε'') for the ceramics sintered at 1200 and 1280 °C, respectively. Inset of Fig. 5.74(b) shows the comparison of dielectric constant at 30 °C over the measured frequencies. Inset of Fig. 5.74(d) demonstrates the Arrhenius plots of the relaxation process.	311
Figure 5.75	XRD patterns of (a) LANO powders and (b) LANO sintered samples.	318
Figure 5.76	SEM images of surface morphologies for (a) LANO-04, (b) LANO-06, and (c) LANO-10 sintered samples.	319
Figure 5.77	EDS spectrum of grain boundary (point 2) for LANO-06 ceramic sample; inset (a) is the fractured surface of the LANO-06 sample; inset (b) is the Al element profile obtained from the EDS spectrum at different measured locations as displayed in the inset (a).	320
Figure 5.78	Temperature dependence of (a) dielectric constant and (b) loss tangent of LANO-04 sample at frequency range of 100 Hz to 5 MHz.	321
Figure 5.79	Frequency dependence of (a) dielectric permittivity and (b) dissipation factor of LANO-04 sample at various temperatures; inset shows the Arrhenius plots of the relaxation process.	322
Figure 5.80	(a) Comparison of impedance spectra for LANO samples at -60 °C and (b) the Arrhenius plots of the grain conduction of LANO samples.	323

LIST OF FIGURES (Cont.)

		Page
Figure 5.81	XRD patterns of $\text{Li}_x\text{Fe}_y\text{Ni}_{1-x-y}\text{O}$ ceramics for the samples of (a) $\text{Fe}_{0.02}\text{Ni}_{0.98}\text{O}$, (b) $\text{Li}_{0.02}\text{Fe}_{0.02}\text{Ni}_{0.96}\text{O}$, (c) $\text{Li}_{0.05}\text{Fe}_{0.02}\text{Ni}_{0.93}\text{O}$, (d) $\text{Li}_{0.10}\text{Fe}_{0.02}\text{Ni}_{0.88}\text{O}$, (e) $\text{Li}_{0.05}\text{Fe}_{0.05}\text{Ni}_{0.90}\text{O}$, and (f) $\text{Li}_{0.05}\text{Fe}_{0.10}\text{Ni}_{0.85}\text{O}$.	327
Figure 5.82	SEM images of surface morphologies for (a) $\text{Fe}_{0.02}\text{Ni}_{0.98}\text{O}$, (b) $\text{Li}_{0.02}\text{Fe}_{0.02}\text{Ni}_{0.96}\text{O}$, (c) $\text{Li}_{0.05}\text{Fe}_{0.02}\text{Ni}_{0.93}\text{O}$, (d) $\text{Li}_{0.10}\text{Fe}_{0.02}\text{Ni}_{0.88}\text{O}$, (e) $\text{Li}_{0.05}\text{Fe}_{0.05}\text{Ni}_{0.90}\text{O}$, and (f) $\text{Li}_{0.05}\text{Fe}_{0.10}\text{Ni}_{0.85}\text{O}$.	328
Figure 5.83	The effect of Li concentration on frequency dependence of (a) dielectric constant and (b) loss tangent for the LFNO ceramics at room temperature.	330
Figure 5.84	The effect of Fe concentration on the frequency dependence of (a) dielectric constant and loss tangent of the LFNO ceramics at room temperature.	331
Figure 5.85	Frequency dependence of dielectric constant and loss tangent for $\text{Li}_{0.02}\text{Fe}_{0.02}\text{Ni}_{0.96}\text{O}$ [(a) and (b)] and $\text{Li}_{0.05}\text{Fe}_{0.10}\text{Ni}_{0.85}\text{O}$ [(c) and (d)] samples at the selected temperatures. The inset of figure (a) and (b) shows frequency dependence of the dielectric constant of $\text{Fe}_{0.02}\text{Ni}_{0.98}\text{O}$ sample at temperature range of 50-190 °C. The inset of figure (c) and (d) shows two Gaussian peaks (blue lines) which are least-squares fitting of experimental data at 100 °C; the red line is fitted result; (1) and (2) are the LFR and HFR, respectively.	334
Figure 5.86	Arrhenius plots of the relaxations of the LFNO ceramics.	335

LIST OF FIGURES (Cont.)

	Page
Figure 5.87 Impedance spectrum of $\text{Li}_{0.02}\text{Fe}_{0.02}\text{Ni}_{0.96}\text{O}$ sample at room temperature; inset shows the impedance spectrum of $\text{Li}_{0.05}\text{Fe}_{0.10}\text{Ni}_{0.85}\text{O}$ sample at room temperature. The vertical lines are used to separate the bulk polarization (1#) and interfacial polarization (2#).	335
Figure 5.88 XRD patterns of $\text{Li}_x\text{Ti}_y\text{Ni}_{1-x-y}\text{O}$ powders and ceramic samples prepared by a PVA method.	339
Figure 5.89 SEM micrographs of $\text{Li}_x\text{Ti}_y\text{Ni}_{1-x-y}\text{O}$ ceramics for the samples of (a) LTNO-05, (b) LTNO-10, and (c) LTNO-20.	340
Figure 5.90 (a) SEM micrograph of the fractured surface of LTNO-05 sample, (b) EDS spectra at point 2 in (a), and (c) Ti element profile obtained from the EDS spectra.	340
Figure 5.91 (a) Temperature dependences of dielectric constant (ϵ') and loss tangent ($\tan\delta$) for LTNO-05 at selected frequencies and (b) the temperature dependence of dielectric constant and loss tangent for LTNO-05, LTNO-10, and LTNO-20 at 1 kHz.	343
Figure 5.92 Frequency dependences of (a) ϵ' and (b) ϵ'' of LTNO-05 at various temperatures. The solid curves are the best fits to equations (5.42) and (5.43) for ϵ' and ϵ'' , respectively, which include both a Cole–Cole relaxation and a complex conductivity contribution. (c) The evolution of the relaxation and dc conductivity contribute to the dielectric loss. (d) Arrhenius plots of the relaxation time and dc conductivities.	348
Figure 5.93 Dielectric constant of (a) $\text{Li}_{0.05}\text{Ti}_{0.02}\text{Ni}_{0.93}\text{O}$ and (b) CuO (CuO-1 sample) ceramics.	351
Figure 5.94 SEM images of CuO ceramics: (a) CuO-1 sintered at 920 °C and (b) CuO-2 sintered at 980 °C.	352

LIST OF FIGURES (Cont.)

		Page
Figure 5.95	(a) The frequency dependence of dielectric constant for CuO-1 at various temperatures; inset (1) shows the frequency dependence of dielectric loss for CuO-1 and inset (2) displays the frequency dependence of dielectric constant for CuO-2. (b) The Arrhenius plot of the dielectric relaxation time for the CuO-1 and CuO-2.	354
Figure 5.96	The frequency dependence of dielectric constant for CuO ceramic at various temperatures; the solid lines represent calculated values of equation (5.18) for a Cole-Cole model.	355

LIST OF SYMBOLS

σ'_{s0}	Surface charge density
\vec{E}	Electric field
ϵ_0	The permittivity of free space ($8.854 \times 10^{-12} \text{ Fm}^{-1}$)
μ_0	The vacuum permeability
c_0	The speed of light in vacuum
ϵ_{permit}	The permittivity of a dielectric material
ϵ'	The dielectric constant
C_0	The capacitance of the free-space capacitor
C	The capacitance
$\vec{\mu}$	The electric dipole moment
$\pm Q$	The electric charges
\vec{P}	The polarization
N	The number of the displaced molecules per unit volume
σ'_b	The bound charge density
I_c	The charging current
V	The sinusoidal voltage ($V = V_0 \exp(j\omega t)$)
G	The conductance
I_{total}	The total current
I_l	The loss current
δ	The loss angle
ϵ^*	The complex dielectric constant
ϵ'	The real part of ϵ^* (the dielectric constant)
ϵ''	The imaginary part of ϵ^* (the dielectric loss)
ω	The angular frequency
$\tan \delta$	The loss tangent or the dissipation factor
\vec{D}	The total electric displacement field
$\epsilon^*_{\text{permit}}$	The complex permittivity of a dielectric material
χ	The electric susceptibility
N_i	The number of dipoles of type i per unit volume
$\bar{\mu}_i$	The average dipole moment
α	The polarizability
E'	The local electric field
E_a	The external applied field
α_e	The electronic polarizability
α_a	The atomic polarizability
α_{or}	The orientational polarizability

LIST OF SYMBOLS (Cont.)

α_{sc}	The space charge polarizability
P_{total}	The total polarization
P_e	The electronic polarization
P_a	The atomic polarization
P_{or}	The orientational polarization
P_{∞}	The high-frequency polarization
ϵ'_{∞}	The dielectric constant at a high frequency range
ϵ'_s	The low-frequency dielectric constant or the relaxed static dielectric constant
τ	The relaxation time
P'	The probability of a jump
z	The valence of the ion
$P_{s(hopping)}$	The zero-frequency value of the hopping polarization
k_B	The Boltzmann constant (1.38×10^{-23} J/K)
T	The absolute temperature (K)
b	The distance separating the potential well
α	The Cole-Cole constant parameter ($0 < \alpha \leq 1$)
J_{total}	The total current density
J	The conduction current or current density
σ_{dc}	The dc electrical conductivity
σ_{ac}	The ac electrical conductivity
Y^*	The complex admittance
E_a	The activation energy
$f_{p(\epsilon^*)}$	The frequencies at the peak of ϵ''
$f_{p(\delta)}$	The frequencies at the peak of $\tan \delta$
Z^*	The complex impedance
Z'	The real part of the complex impedance
Z''	The imaginary part of the complex impedance
(R_g, R_{gb})	The resistances of grains and grain boundaries, respectively
(C_g, C_{gb})	The capacitances of grains and grain boundaries, respectively
ϵ'_{gb}	The dielectric constant of the grain boundary
d_g	The grain size
d_{gb}	The thickness of grain boundary
$\sigma_{polaron}$	The polaron conductivity

LIST OF SYMBOLS (Cont.)

E_g	The activation energy for conduction inside grain
E_{gb}	The activation energy for conduction at grain boundary
$Ti_{Ni}^{\bullet\bullet}$	The Ti ion sitting on the Ni lattice site with two positive charges
V_{Ni}''	The Ni vacancy with double negative charge
ϵ_g^*	The complex dielectric permittivity of grain
ϵ_{gb}^*	The complex dielectric permittivity of grain boundary
$Ta_{Ni}^{\bullet\bullet\bullet}$	The Ta ion sitting on the Ni lattice site with three positive charges
Li'_{Ni}	The Li ion sitting on the Ni lattice with a single negative charge
$V_o^{\bullet\bullet}$	The oxygen vacancy with double positive charges
$[V_o^{\bullet\bullet}]$	The concentration of oxygen vacancy
$Ni_i^{\bullet\bullet}$	The Ni ion in the interstitial lattice site
K	The equilibrium constant
X	The reactance
G	The conductance
B	The susceptance
D	The dissipation factor
R	The resistance
C_p	The capacitance of the parallel plate capacitor
F	The structure factor
f	The atomic scattering factor
D	The diffusion coefficient or diffusivity
G_L	The limiting grain size
r	The radius of the including particles
C_s	The capacitance of surface layer
R_s	The resistance of surface layer